Revision 2

High-pressure electrical conductivity and elasticity of iron-bearing δ-AlOOH

Xiaowan Su[1], Jin Liu[2,3,*], Yukai Zhuang[2,4], Chaojia Lv[2], Xuyong Pang[5], Fuyang Liu[2], Xiaohui Yu[6], Qiang Sun[1,*]

[1]*School of Earth and Space Sciences, Peking University, Beijing 100871, China*
[2]*Center for High Pressure Science and Technology Advanced Research (HPSTAR), Beijing 100094, China*
[3]*CAS Center for Excellence in Deep Earth Science, Guangzhou, 510640, China*
[4]*Institute of Atomic and Molecular Physics, Sichuan University, Chengdu 610065, China*
[5]*Institute of Mineral Resources, Chinese Academy of Geological Sciences, Beijing 100037, China*
[6]*Beijing National Laboratory for Condensed Matter Physics, Institute of Physics, Chinese Academy of Sciences, Beijing 100190, China*
*Correspondence to: J. Liu (jin.liu@hpstar.ac.cn) and Q. Sun (qiangsun@pku.edu.cn)

Research Highlights:

(1) Electrical conductivity and compressibility were determined for δ-(Al,Fe)OOH with 5 and 48 mol.% FeOOH at pressures up to 75 GPa.

(2) The conductivity of δ-(Al,Fe)OOH may be slightly affected by high iron content and spin transition at high pressure.

(3) Subducted Fe-bearing δ-AlOOH may account for some high conductivity regions in the lower mantle, e.g., the North Philippine Sea slab.

DOI: https://doi.org/10.2138/am-2022-8393. http://www.minsocam.org/

Abstract

The electrical conductivity and elasticity of deep hydrous phases are essential to constrain water distribution, as well as decipher the origins of conductivity anomalies in the lower mantle. To uncover the impact of iron-bearing δ-AlOOH on geophysical properties of the lower mantle, we carried out synchrotron x-ray diffraction and electrical conductivity measurements on δ-$(Al_{0.52}Fe_{0.48})OOH$ and $(Al_{0.95}Fe_{0.05})OOH$ in diamond-anvil cells at pressures up to 75 GPa at room temperature. A sharp volume reduction of ~ 6.5% was observed in δ-$(Al_{0.52}Fe_{0.48})OOH$ across the spin transition at 40.8–43.3 GPa, where its electrical conductivity increases steadily without abrupt changes. The electrical conductivity of δ-$(Al_{0.52}Fe_{0.48})OOH$ is greater than that of pure δ-AlOOH at high pressure, suggesting that both small polaron and proton conduction mechanisms dominate in iron-bearing δ-AlOOH. Furthermore, the high-pressure electrical conductivity profiles are comparable between δ-$(Al_{0.95}Fe_{0.05})OOH$ and δ-$(Al_{0.52}Fe_{0.48})OOH$, indicating that high iron content only marginally influence the conductivity of iron-bearing δ-AlOOH. Notably, the electrical conductivity of iron-bearing δ-AlOOH along the North Philippine geotherm is greater than the average 1D electrical conductivity profile in the mantle (*Ohta et al.,* 2010a). This result suggests that δ-(Al,Fe)OOH is a promising candidate to account for high conductivity in some subducting slabs.

Keywords: Hydrous minerals, Spin transition, High pressure, X-ray diffraction, Electrical conductivity

1. Introduction

Knowledge of water distribution in the mantle is fundamental to understand our planet's evolution and geodynamics (*Mao and Mao,* 2020; *Ohtani,* 2020). It is widely believed that water is transported to the lower mantle via slab subduction in the forms of various hydrous phases such as δ-AlOOH (*Duan et al.,* 2018; *Sano-Furukawa et al.,* 2008), phase D (*Pamato et al.,* 2015), phase H (*Liu et al.,* 2019b), $(FeH)_{1-x}Ti_xO_2$ (*Nishihara et al.,* 2016), pyrite-type $(Mg,Fe)O_2H_x$ (*Hu et al.,* 2021), and hexagonal $(Mg,Fe)_2O_{3+\delta}H_x$ (*Liu et al.,* 2021). The δ-AlOOH phase, one of the most important hydrous minerals in subducting slabs, is stable at least up to 134 GPa and 2300 K, that is at the high pressure and temperature (*P-T*) conditions of the Earth's lowermost mantle (*Duan et al.,* 2018; *Sano-Furukawa et al.,* 2008). Thus, it has been considered as an important deep-water carrier throughout the lower mantle (*Ohtani et al.,* 2001; *Sano-Furukawa et al.,* 2008; *Tsuchiya and Tsuchiya,* 2011). Additionally, δ-AlOOH forms a solid solution with the isostructural hydrous phase ε-FeOOH in multicomponent systems (*Kawazoe et al.,* 2017; *Ohira et al.,* 2019; *Liu et al.,* 2019b; *Buchen et al.,* 2021).

The incorporation of FeOOH greatly influences the physics and chemistry of δ-AlOOH. Because of pressure effects on the electronic spin states of *3d* transition metal iron, the δ-(Al,Fe)OOH phase undergoes a high-spin to low-spin (HS-LS) transition of iron at ~ 40 GPa (*Ohira et al.,* 2019; *Hsieh et al.,* 2020; *Su et al.,* 2021a). Intriguingly, the unit cell volume, compressibility, and thermal conductivity of δ-(Al,Fe)OOH exhibit abnormal behaviors throughout the electronic spin-pairing transition. For instance, δ-$(Al_{0.908}Fe_{0.045})OOH_{1.14}$ and δ-$(Al_{0.832}Fe_{0.117})OOH_{1.15}$ both display gradual volume collapses across the HS-LS transition (*Ohira et al.,* 2019). The thermal conductivity of δ-$(Al_{0.85}Fe_{0.15})OOH$ drastically decreases at 30–45 GPa and approaches an exceptionally low value of ~ 10 W m^{-1} K^{-1} in the LS state at 66 GPa (*Hsieh et al.,* 2020). Moreover, the incorporation of 5 mol.% FeOOH decreases the shear-wave velocity of δ-AlOOH by ~ 5% at 20–135 GPa (*Su et al.,* 2021b). However, the effect of iron on the electrical conductivity of δ-AlOOH has not yet been reported under high pressures.

The electrical conductivity values of iron-free δ-AlOOH remain almost the same up to 50

GPa, which indicates proton conduction is the primary conduction mechanism (*Zhuang et al.,* 2021). ε-FeOOH exhibits much higher conductivity than δ-AlOOH up to 20 GPa at high temperatures (*Wang and Yoshino*, 2021). We note that the electrical conductivity of mantle minerals would be affected by the spin transition of iron at high pressure. In particular, bridgmanite and ferropericlase are subject to conductivity reduction across iron spin transition (*Lin et al.,* 2007; *Ohta et al.,* 2010b). It has been ascribed to the reduced unpaired electrons, which are the charge transfer carriers in the small polaron conduction mechanism. Thus, the incorporation of FeOOH and iron spin transition are expected to influence the electrical behavior of δ-AlOOH with increasing pressure. Meanwhile, it still remains unclear whether the presence of this hydrous phase could contribute to conductivity anomalies observed in the deep mantle, which, in turn, can allow a better understanding of the Earth's deep-water cycle. Therefore, high-pressure electrical conductivity measurements are highly demanded for iron-bearing δ-AlOOH.

In this work, δ-$(Al_{0.95}Fe_{0.05})OOH$ and δ-$(Al_{0.52}Fe_{0.48})OOH$ single-crystal samples were synthesized at 26 GPa and 1473 K for 4 hours using a 1000-ton Kawai-type multi anvil apparatus. Electrical conductivity measurements were conducted on these two samples up to 66.3 and 68.3 GPa at room temperature, respectively, in diamond-anvil cells (DAC). In addition, the pressure-volume relation of δ-$(Al_{0.52}Fe_{0.48})OOH$ was investigated at pressures to 75.4 GPa using synchrotron x-ray diffraction (XRD). These results are used to decipher how iron content and spin transition affect the electrical conductivity of iron-bearing δ-AlOOH at high pressure. Our study gives insights into the electrical structure of the deep mantle, e.g., beneath northeast China and the North Philippine Sea.

2. Experimental Methods

2.1 Sample synthesis and characterization

High *P-T* synthesis experiments were performed in a 1000-ton Kawai-type multi anvil apparatus at the Institute of Physics, Chinese Academy of Sciences, Beijing. Details of the synthesis procedure were similar to those described by *Kawazoe et al*. (2017) and *Ohira et al*.

(2019). Fe_2O_3 and $Al(OH)_3$ powders were mixed as starting materials with chemical compositions of $(Al_{1-x}Fe_x)OOH$ and excess water, where x = 0.50 and 0.05, respectively. A welded Au capsule was filled with powder mixtures. The capsule was placed in the MgO cylinder, and the rhenium heater was enclosed by a ZrO_2 thermal insulator. A Cr_2O_3-doped MgO octahedron with a 10 mm edge length was used as the pressure medium. Tungsten carbide second-stage anvils were used with a 4 mm edge length. The temperature was measured using a $W_{97\%}Re_{3\%}$-$W_{75\%}Re_{25\%}$ thermocouple (type D). The assembly was first compressed to 26 GPa and then heated to 1473 K. This target temperature was maintained for 4 hours for grain growth. The sample was rapidly quenched at 26 GPa by switching off the electrical power and then slowly decompressed for 15 hours.

The chemical compositions of the recovered samples were measured using electron probe microanalyzer (EPMA) at the Institute of Mineral Resources, Chinese Academy of Geological Sciences, resulting in $(Al_{0.52}Fe_{0.48})OOH$. The recovered samples with the lower iron content were examined using SEM-EDS (scanning electron microscope equipped with energy-dispersive spectrometer) at Peking University, resulting in $(Al_{0.95}Fe_{0.05})OOH$. SEM and EPMA analyses showed that the synthesized samples are chemically homogeneous within analytical uncertainties. XRD patterns of the recovered samples were collected using Bruker APEX III D8 venture diffractometer at the Center for High Pressure Science and Technology Advanced Research (HPSTAR). The lattice parameters of $(Al_{0.52}Fe_{0.48})OOH$ (space group: $P2_1nm$) are a = 2.9078(3) Å, b = 4.3274(5) Å, and c = 4.8223(6) Å. In addition, $(Al_{0.95}Fe_{0.05})OOH$ (denoted as "Delta95") has an orthorhombic structure (space group: $P2_1nm$), yielding the unit cell parameters of a = 2.8465(2) Å, b = 4.2448(2) Å, and c = 4.7350(3) Å. These values are consistent with the previous studies (*Su et al.,* 2021b; *Buchen et al.,* 2021; *Ohira et al.,* 2019; *Sano-Furukawa et al.,* 2009; *Suzuki et al.,* 2010). Figure 1 shows the unit-cell parameters of δ-(Al,Fe)OOH samples increasing with Fe/(Al+Fe) at ambient conditions.

2.2 Synchrotron x-ray diffraction experiments

δ-($Al_{0.52}Fe_{0.48}$)OOH (denoted as "Delta52") samples were double-side polished to ~ 40 μm in diameter and 7–9 μm thick. The prepared platelet was then loaded into a sample chamber of100 μm in diameter and ~ 25 μm thick, drilled into the center of the pre-indented tungsten gasket in a DAC. Au and ruby were placed next to the sample to serve as pressure calibrants (*Fei et al.,* 2007; *Mao et al.,* 1986). Neon was loaded into the sample chamber as the pressure-transmitting medium using the high-pressure gas loading system at HPSTAR. *In situ* synchrotron XRD experiments were conducted at the BL10XU beamline of the SPring-8 synchrotron radiation facility (*Hirao et al.,* 2020). An x-ray beam with λ = 0.4133 Å was used in combination with an image plate (IP) detector (Rigaku RAXIS-IV). The six diffraction peaks (110, 101, 200, 111, 210, 211) were observed in most of the diffraction patterns of the Delta52, whereas other peaks were relatively weak. Therefore, these six diffraction peaks of the Delta52 were used to calculate the lattice parameters via the Unit Cell and Dioptas programs (*Prescher and Prakapenka,* 2015). Based on XRD patterns of the loaded sample at ~1.0 GPa, the single-crystal Delta52 sample was crushed to a large-grained polycrystalline sample in closing the diamond anvil cell.

2.3 Electrical conductivity measurements

The values of electrical conductivity of the Delta52 and Delta95 samples were determined up to 66.3 and 68.3 GPa, respectively, at room temperature by using symmetrical DACs with a culet size of 250 μm. Delta52 and Delta95 samples were prepared into sample disks of 40 μm in diameter and ~ 8 μm thick. Re gaskets were pre-indented to 35–40 μm (c.a. 20 GPa) thick between a pair of diamond anvils, and a hole of 180 μm in diameter was drilled into the center of the pre-indention. A powder mixture of cubic boron nitride (cBN) and epoxy was packed into the hole and further compressed up to 20-25 GPa. A 100 μm diameter hole was then drilled into the center of the cBN-epoxy gasket insert. The sample disk was further placed into the hole, and four platinum electrodes were connected to the sample. The electrical resistance of the sample was measured by using Solartron-1260 AC impedance spectroscopy with frequencies between 0.1 Hz and 10 MHz using the four-terminal method (*Zhuang et al.,* 2021). The procedure of resistance data analysis can be found in detail in *van der Pauw* (1958).

3. Results and Discussion

3.1 Compressibility and spin transition of iron-bearing δ-AlOOH at high pressure

XRD patterns of the Delta52 were collected up to 75.4 GPa (Fig. 2). The lattice parameters (*a*, *b*, and *c*) and unit cell volume were determined for the Delta52 (Fig. 3 and Table 1). The pressure-volume (*P-V*) compression data of the Delta52 were divided into three regions based on our x-ray emission scattering (XES) and laser Raman spectroscopic results on analogous material (*Su et al.,* 2021a): 0–10.4 GPa for the $P2_1nm$ structure (HS), 10.4–40.8 GPa for the *Pnnm* structure (HS), and 43.3–75.4 GPa for the *Pnnm* structure (LS). The third-order Birch-Murnaghan (BM) EoS was fitted to the *P-V* data of the Delta52 using EosFit7Gui software (*Gonzalez-Platas et al.,* 2016). The unit cell volume at ambient pressure conditions (V_0), isothermal bulk modulus (K_{T0}), and pressure derivative of the bulk modulus (K_{T0}') were derived, yielding: V_0 = 61.6(1) Å^3, K_{T0} = 134(4) GPa, and K_{T0}' fixed at 4 for the $P2_1nm$ structure (HS); V_0 = 60.4(1) Å^3, K_{T0} = 216(2) GPa, and K_{T0}' = 3.98(9) for the *Pnnm* structure (HS); and V_0 = 56.5(1) Å^3, K_{T0} = 234(2) GPa, and K_{T0}' = 4.00(2) for the *Pnnm* structure (LS) (Table 2).

The *P-V* profile of the Delta52 shows a sharp volume reduction of ~ 6.5% in a narrow pressure range between 40.8 and 43.3 GPa at 300 K in Ne pressure medium (Fig. 3 and Table 3). Such a volume collapse is related to the pressure-induced spin transition in the Delta52, whereas a gradual volume collapse of ~ 10.3% was observed in ε-FeOOH at ~45(2) GPa (*Thompson et al.,* 2017). The volume reductions are about 1.3% for δ-$(Al_{0.95}Fe_{0.05})OOH$ and δ-$(Al_{0.908}Fe_{0.045})OOH_{1.14}$ and 2.8% for δ-$(Al_{0.832}Fe_{0.117})OOH_{1.15}$ across the spin transition (*Ohira et al.,* 2019; *Su et al.,* 2021b). In other words, the volume reduction of the δ-(Al, Fe)OOH increases with increasing FeOOH content throughout the spin transition of iron (Table 3). On the other hand, a thermal conductivity anomaly of δ-$(Al_{0.97}Fe_{0.03})OOH$ was observed at 30–50 GPa and room temperature using silicon oil as a pressure-transmitting medium by *Hsieh et al.* (2020), which has also been related to the spin crossover. Similarly, δ-$(Al_{0.88}Fe_{0.12})OOH$ and δ-$(Al_{0.85}Fe_{0.15})OOH$ with higher iron contents exhibit anomalous changes in thermal conductivity approximately at 30–53 GPa (*Hsieh et al.,* 2020). Notably, the use of neon as a pressure-transmitting medium in this study can greatly decrease the width of the spin crossover of iron in δ-(Al,Fe)OOH, while the use of silicone oil generates a larger deviatoric stress that could broaden the width of iron spin transition. Overall, the onset pressure of the spin transition appears to increase gradually with the increasing iron content from 3 to 48 mol.%, approximately from 30 to 41 GPa (*Su et al.,* 2021a).

Figure 4 presents the volume difference between the Delta52 and δ-AlOOH as a function of pressure at room temperature (Sano-Furukawa et al., 2009). It decreases dramatically at ~ 40 GPa and approaches 1 $Å^3$ at 65 GPa. The unit cell volume of the Delta52 is close to that of δ-AlOOH above 40 GPa, illustrating that the effective ionic radius of ferric iron Fe^{3+} in the LS state is almost the same as that of Al^{3+}. In addition, at approximately 10 GPa, the *a/c* and *b/c* ratio values of the Delta52 reach their minima, whereas the *a/b* ratio values reach their maximum (Fig. 5). Such trends were also observed for the axial ratios of δ-$(Al_{0.832}Fe_{0.117})OOH_{1.15}$, δ-$(Al_{0.908}Fe_{0.047})OOH_{1.14}$, and δ-AlOOH at ~ 10 GPa (*Ohira et al.,* 2019; *Su et al.,* 2021b; *Sano-Furukawa et al.,* 2009; *Duan et al.,* 2018). Similarly, the reversal of the axial ratios' pressure dependences was observed for δ-$(Al_{0.95}Fe_{0.05})OOH$ at around 14 GPa (*Su et al.,* 2021b). This behavior has been related to the hydrogen bond order-disorder phase transition from $P2_1nm$ to *Pnnm* (*Sano-Furukawa et al.,* 2018; *Su et al.,* 2021b; *Ohira et al.,* 2019). In contrast, the pressure dependences of ε-FeOOH axial ratios are different due to the absence of the hydrogen bond order-disorder phase transition. The K_{T0} value of the Delta52 increases by about 52.7% at 10.4–13.3 GPa and 7.6% at 40.8–43.3 GPa, respectively (Fig. 6a). These results show that both the hydrogen bond order-disorder and HS-LS phase transitions influence the compressibility of iron-bearing δ-AlOOH.

The bulk sound velocity of the Delta52 as a function of pressure is shown in Figure 6b. The velocity of the Delta52 increases monotonically from 15 to 75 GPa. Compared to δ-AlOOH, the substitution of 48 mol.% FeOOH decreases the velocity by ~ 7.3%. Similarly, the bulk sound velocity of the δ-($Al_{0.87}Fe_{0.13}$)OOH is 4.0% lower than that of δ-AlOOH at 65 GPa (*Ohira et al.,* 2021). Additionally, the bulk sound velocity of the Delta95 is less than that of δ-AlOOH by ~ 2.9% at 20–135 GPa (*Su et al.,* 2021b). Moreover, ε-FeOOH decreases the velocity by ~ 16.3% with respect to δ-AlOOH. Thus, the magnitude of the velocity reduction in δ-(Al,Fe)OOH exhibits a positive correlation with iron content. On the other hand, the bulk sound velocity of δ-(Al,Fe)OOH does not undergo a dramatic change across the spin crossover, although the spin transition increases the bulk modulus (Fig. 6b). The reason for this is that it is counterbalanced by the increased density of δ-(Al,Fe)OOH from the HS to LS states.

3.2 Electrical conductivity and conduction mechanisms of δ-(Al,Fe)OOH at high pressure

The electrical conductivity of the Delta52 and Delta95 is shown as a function of pressure in Figure 7a and Table 4. The electrical conductivity profile of the Delta95 is present with a positive spike of ~ $10^{-1.50}$ S/m at around 6 GPa (Fig. 7a). This abrupt change may be related to the hydrogen bond order-disorder transition, which would weaken the O–H bond and strengthen the H···O bond (*Kuribayashi et al.,* 2014; *Cortona,* 2017; *Ohira et al.,* 2019; *Wang and Yoshino,* 2021). Moreover, the electrical conductivity of the Delta95 increases with increasing pressure at 10–66 GPa (Fig. 7a). We note that δ-($Al_{0.85}Fe_{0.15}$)OOH (denoted as "Delta85") shows two new Raman bands at 6.0 GPa, in agreement with the transition from an ordered ($P2_1nm$) to a disordered hydrogen bonding structure (*Pnnm*) for δ-AlOOH and the Delta95 (*Su et al.*, 2021a). In this previous study, the Delta52 exhibits two new Raman bands between 8.5 and 15.8 GPa, suggesting that the incorporation of 48 mol.% FeOOH would increase the order-disorder transition pressure. Thus, like the Delta95, it is expected to observe a dramatic change in the electrical conductivity of the Delta52 at 8.5–15.8 GPa. However, it is not present in the present measurements due to limited data points that were collected below 20 GPa. The conductivity of the Delta52 increases with pressure from $10^{-1.56}$ S/m at 23 GPa to $10^{-0.69}$ S/m at 68 GPa (Fig. 7a). The electrical conductivity of iron-free δ-AlOOH is around $10^{-2.25}$ S/m and remains nearly unchanged with increasing pressure up to ~ 50 GPa (*Zhuang et al.,* 2021). That is, the incorporation of FeOOH significantly alters the electrical conductivity evolution of δ-AlOOH at pressures greater than 20 GPa. Moreover, the electrical conductivity values of the Delta52 and Delta95 monotonically increase without kinks throughout the spin crossover (Fig. 7a). This suggests that the iron spin transition may have negligible effects on the electrical conductivity of iron-bearing δ-AlOOH at high pressure. In general, iron spin transition greatly reduces unpaired electrons and thus the charge carrier density in the small polaron conduction mechanism; accordingly, mantle bridgmanite and ferropericlase undergo a reduction in electrical conductivity from the HS to LS states (*Lin et al.,* 2007; *Ohta et al.,* 2010b). This reduction, however, does not occur in δ-(Al,Fe)OOH, indicating that the spin transition-induced decrease in charge carrier density may not alter the predominant electrical conductivity mechanism of δ-(Al,Fe)OOH at high pressure.

Proton conduction is well known to be present in hydrous minerals owing to high proton mobility (*Guo,* 2016). The number of free protons in hydrous phases and proton migration rate through lattice sites are two significant factors influencing their conductive behavior. The O_1–H···O_2 bonds of δ-AlOOH become symmetric above 20 GPa, hindering protons moving freely (*Wang and Yoshino,* 2021). Therefore, the electrical conductivity values of δ-AlOOH keep almost constant at 20–50 GPa (*Zhuang et al.,* 2021). Notably, the electrical conductivity values of δ-(Al,Fe)OOH become greater than that of pure δ-AlOOH at pressures greater than 20 GPa. It is mostly related to the increment of free protons in iron-bearing δ-AlOOH through the activation reaction of $Fe^{3+} = Fe^{2+} + H^+$. The δ-(Al,Fe)OOH may thus contain a number of Fe^{2+} through this substitution mechanism. Small polaron hopping conduction occurs through charge transfer between neighboring ions of different valences like Fe^{2+} and Fe^{3+} or electron-electron hole pair recombination. As *Wang and Yoshino* (2021) pointed out, the dynamical coexistence of Fe^{2+} and Fe^{3+} in δ-(Al,Fe)OOH makes further contributions to the conductivity. Therefore, the primary conduction mechanism of δ-(Al,Fe)OOH at 20–70 GPa is proton conduction coupled with small polaron hopping conduction. It is the same as the conduction mechanisms of iron-bearing antigorite, an important hydrous mineral in subduction zones (*Guo et al.,* 2011).

The electrical behavior of δ-AlOOH is greatly altered by the incorporation of FeOOH at high pressure. At 20–70 GPa, the electrical conductivity values of iron-bearing δ-AlOOH phases are greater than that of pure δ-AlOOH (Fig. 7a). Specifically, the electrical conductivity of δ-AlOOH at 50 GPa is enhanced by about 25 times through the incorporation of 48 mol.% FeOOH, corresponding to an increase of ~ 1.4 in decimal logarithm unit. Moreover, the linear fitting between 20–70 GPa yields a pressure dependence of the decimal logarithm of electrical conductivity 0.02–0.03 log[S/m] per gigapascal for the Delta52 and Delta95 at room temperature (Fig. 7b). We note that the Delta52 and Delta95 have comparable electrical conductivity values at pressures greater than 20 GPa. That is, the electrical conductivity behavior of iron-bearing δ-AlOOH may be slightly affected by FeOOH content between 5 and 48 mol.%. Similarly, it has been observed on the thermal conductivity of δ-(Al,Fe)OOH with 3–15 mol.% FeOOH above 40–50 GPa (*Hsieh et al.,* 2020).

4. Implications

Aluminous hydrous mineral δ-AlOOH may be stable up to the deep lower mantle conditions based on the recent XRD experiments at high *P-T* conditions (*Duan et al.,* 2018). Diaspore (α-AlOOH), a naturally occurring hydrous mineral in sediments, could transform into its high-pressure phase (δ-AlOOH) when being transported to deep Earth through subducting slabs (*Suzuki et al.,* 2000). We note that δ-AlOOH could also emerge out of the decomposition of Al-rich phase D and phase Egg ($AlSiO_3OH$) at the uppermost lower mantle conditions (*Sano et al.,* 2004; *Xu and Inoue,* 2019). In addition, δ-AlOOH likely coexists with bridgmanite and remains stable down to the bottom of the lower mantle (*Ohira et al.,* 2014). More importantly, δ-AlOOH is expected to accommodate some FeOOH in the deep mantle. *Wang and Yoshino* (2021) suggested that δ-(Al,Fe)OOH could be entrained into the deep mantle through the North Philippine Sea slabs. *Liu et al.* (2019b) experimentally synthesized a series of Al-rich hydrous phases up to 15–17 vol% out of subducted oceanic crusts in the mantle, and found that

(Al,Fe)OOH components are predominant according to their large volume press experiments at 25–26 GPa and high temperatures. Therefore, the δ-(Al,Fe)OOH phase is likely stable in cold subducting slabs when entering the lower mantle.

Furthermore, the electrical conductivity of the δ-(Al,Fe)OOH was extrapolated to high *P-T* conditions, allowing us to assess how the δ-(Al,Fe)OOH phase contributes to the electrical structure of the lower mantle (Figs 7b and 8). *Wang and Yoshino* (2021) reported the activation enthalpy (*ΔH*) of δ-(Al,Fe)OOH with 0.82 wt% Fe_2O_3 is 0.38(1) eV at 500–1200 K and 20 GPa. Assuming that the activation enthalpy of δ-(Al,Fe)OOH would not change significantly with increasing pressure, the pressure dependence on electrical conductivity of δ-(Al,Fe)OOH could not change with increasing temperature. Thus, the pressure dependence of the decimal logarithm of electrical conductivity of δ-(Al,Fe)OOH could be extrapolated from at 300 K to higher temperatures in this study. The electrical conductivity of the δ-(Al,Fe)OOH along the cold slab geotherm (e.g., the North Philippine Sea) was calculated using Arrhenius formula (Fig. 8). The extrapolated EC values of δ-(Al,Fe)OOH at depths of ~ 600 km could well match the conductivity-depth profile of δ-(Al,Fe)OOH by *Wang and Yoshino* (2021). Notably, the electrical conductivity values of δ-(Al,Fe)OOH are greater than the average 1D electrical conductivity profile in the range of 600–1500 km (*Ohta et al.,* 2010b). It is conceivable that δ-(Al,Fe)OOH-bearing domains in cold slabs may account for some high conductivity regions in the lower mantle. Meanwhile, the incorporation of some FeOOH would significantly reduce the sound velocity of δ-AlOOH, iron-bearing δ-AlOOH would have sound velocities much lower than major lower-mantle minerals (*Su et al.,* 2021b; *Fu et al.,* 2018). Therefore, iron-bearing δ-AlOOH is a promising candidate contributing to lower-mantle mantle seismic heterogeneities, such as large low-shear-velocity provinces (LLSVPs) and ultralow velocity zones (ULVZs) (*Liu et al., 2017; Mashino et al., 2016; Thompson et al.,* 2017). More interestingly, δ-(Al,Fe)OOH could account for the high conductivity layer and seismic anomalies at similar depths, including Northeast China, East Africa, and the Philippine Sea (*Tarits et al.,* 2010; *Tada et al.,* 2014). In turn, these results may serve as a means of locating deep-water reservoirs in the mantle.

Acknowledgments

This study is funded by the National Key Research and Development Program of China (2019YFA0708502). Y. Zhuang is supported by the China Postdoctoral Science Foundation (18NZ021-0213-216308). J. Liu acknowledges support from the National Natural Science Foundation of China (Grant no. 42072052 and U1930401). We thank Bingmin Yan, Hu Tang, Jiuhua Chen, and Shuailing Ma for providing their technical support for the multi-anvil press experiments, as well as Saori Kawaguchi and Naohisa Hirao for their assistance with synchrotron XRD experiments. *In situ* XRD measurements were performed at the BL10XU beamline of SPring-8 (Proposal 2019A1284 and 2019B1203). SPring-8 is supported by the National Science Foundation Earth Sciences (Grant No. EAR1128799) and the Department of Energy-GeoSciences (Grant No. DE-FG02-94ER14466). Some experiments are supported by the Synergic Extreme Condition User Facility (SECUF).

References

Buchen, J., Sturhahn, W., Ishii, T., and Jackson, J.M. (2021), Vibrational anisotropy of δ-(Al,Fe)OOH single crystals as probed by nuclear resonant inelastic X-ray scattering, *European Journal of Mineralogy*, 33(4), 485-502.

Cortona, P. (2017), Hydrogen bond symmetrization and elastic constants under pressure of δ-AlOOH, *Journal of Physics: Condensed Matter*, 29(32), 325505.

Duan, Y., Sun, N., Wang, S., Li, X., Guo, X., Ni, H., et al. (2018), Phase stability and thermal equation of state of δ-AlOOH: Implication for water transportation to the deep lower mantle, *Earth Planetary Science Letters*, 494, 92-98.

Fei, Y., Ricolleau, A., Frank, M., Mibe, K., Shen, G., Prakapenka, V. Toward an Internally Consistent Pressure Scale, *Proceeding of the National Academy of Sciences*, 104, 9182-9186.

Fu, S., Yang, J., Zhang, Y., Okuchi, T., McCammon, C., Kim, H. I., et al. (2018), Abnormal Elasticity of Fe-bearing Bridgmanite in the Earth's Lower Mantle, *Geophysical Research Letters*, 45(10), 4725-4732.

Gleason, A. E., Quiroga, C. E., Suzuki, A., Pentcheva, R., Mao, W. L. (2013), Symmetrization driven spin transition in ε-FeOOH at high pressure, *Earth and Planetary Science Letters*, 379, 49-55.

Gonzalez-Platas, J., Alvaro, M., Nestola, F., Angel, R. (2016), EosFit7-GUI: a new graphical user interface for equation of state calculations, analyses and teaching, *Journal of Applied Crystallography*, 49(4), 1377-1382.

This is the peer-reviewed, final accepted version for American Mineralogist, published by the Mineralogical Society of America.
The published version is subject to change. Cite as Authors (Year) Title. American Mineralogist, in press.
DOI: https://doi.org/10.2138/am-2022-8393. http://www.minsocam.org/

Guo, X. (2016), Experimental study of the electrical conductivity of hydrous minerals in the crust and the mantle under high pressure and high temperature, *Science China Earth Sciences*, 59(4), 696-706.

Guo, X., Yoshino, T., Katayama, I. (2011), Electrical conductivity anisotropy of deformed talc rocks and serpentinites at 3 GPa, *Physics of the Earth Planetary Interiors*, 188(1-2), 69-81.

Hirao, N., Kawaguchi, S. I., Hirose, K., Shimizu, K., Ohtani, E., Ohishi, Y. (2020), New developments in high-pressure X-ray diffraction beamline for diamond anvil cell at SPring-8, *Matter and radiation at extremes*, 5(1), 018403.

Hsieh, W. P., Ishii, T., Chao, K. H., Tsuchiya, J., Deschamps, F., Ohtani, E. (2020), Spin transition of iron in δ-(Al, Fe)OOH induces thermal anomalies in Earth's lower mantle, *Geophysical Research Letters*, 47(4), 087036.

Hu, Q., Liu, J., Chen, J., Yan, B., Meng, Y., Prakapenka, V. B., et al. (2021), Mineralogy of the deep lower mantle in the presence of H_2O, *National Science Review*, 8(4), nwaa098.

Kawazoe, T., Ohira, I., Ishii, T., Ballaran, T. B., McCammon, C., Suzuki, A., et al. (2017), Single crystal synthesis of δ-(Al,Fe)OOH, *American Mineralogist*, 102(9), 1953-1956.

Kuribayashi, T., Sano-Furukawa, A., Nagase, T. (2014), Observation of pressure-induced phase transition of δ-AlOOH by using single-crystal synchrotron X-ray diffraction method, *Physics Chemistry of Minerals*, 41(4), 303-312.

Lin, J.-F., S. T. Weir, D. D. Jackson, W. J. Evans, Y. K. Vohra, W. Qiu, and C.-S. Yoo (2007), Electrical conductivity of the lower-mantle ferropericlase across the electronic spin transition, *Geophysical Research Letters*, 34(16), L16305.

Liu, J., Lin, J. F., Mao, Z., Prakapenka, V. B. (2014), Thermal equation of state and spin transition of magnesiosiderite at high pressure and temperature, *American mineralogist*, 99(1), 84-93.

Liu, J., Wang, C., Lv, C., Su, X., Liu, Y., Tang, R., et al. (2021), Evidence for oxygenation of Fe-Mg oxides at mid-mantle conditions and the rise of deep oxygen, *National Science Review*, 8(4), nwaa096.

Liu, J., Hu, Q., Kim, D. Y., Wu, Z., Wang, W., Yuming, et al. (2017), Hydrogen-bearing iron peroxide and the origin of ultralow-velocity zones, *Nature*, 551(7681), 494-497.

Liu, J., Hu, Q., Bi, W., Yang, L., Xiao, Y., Chow, P., et al. (2019a), Altered chemistry of oxygen and iron under deep Earth conditions, *Nature Communications*, 10(1), 153-153.

Liu, X., Matsukage, K. N., Nishihara, Y., Suzuki, T., Takahashi, E. (2019b). Stability of the hydrous phases of Al-rich phase D and Al-rich phase H in deep subducted oceanic crust. *American Mineralogist*, 104(1), 64–72.

Mao, H.-k., Xu, J,-A., and Bell, P. (1986), Calibration of the ruby pressure gauge to 800 kbar under quasi-hydrostatic conditions. *Journal of Geophysical Research*, 91, 4673-4676.

Mao, H.-k., and Mao, W. L. (2020), Key problems of the four-dimensional Earth system. *Matter and Radiation at Extremes*, 5(3), 038102.

Mashino, I., Murakami, M., Ohtani, E. (2016), Sound velocities of δ-AlOOH up to core-mantle boundary pressures with implications for the seismic anomalies in the deep mantle, *Journal of Geophysical Research: Solid Earth*, 121(2), 595-609.

Nishihara, Y., Matsukage, K.N. (2016), Iron-titanium oxyhydroxides as water carriers in the Earth's deep mantle, American Mineralogist,101(4), 919-927.

Ohira, I., Ohtani, E., Sakai, T., Miyahara, M., Hirao, N., Ohishi, Y., and Nishijima, M. (2014), Stability of a hydrous δ-phase, AlOOH-$MgSiO_2(OH)_2$, and a mechanism for water transport into the base of lower mantle, *Earth and Planetary Science Letters*, 401, 12-17.

Ohira, I., Jackson, J. M., Solomatova, N. V., Sturhahn, W., Finkelstein, G. J., Kamada, S., et al. (2019), Compressional behavior and spin state of δ-(Al, Fe) OOH at high pressures, *American Mineralogist*, 104(9), 1273-1284.

Ohira, I., Jackson, J. M., Sturhahn, W., Finkelstein, G. J., Kawazoe, T., Toellner, T. S., et al. (2021), The influence of δ-(Al,Fe)OOH on seismic heterogeneities in Earth's lower mantle, *Scientific Reports*, 11, 12036.

Ohta, K., Hirose, K., Ichiki, M., Shimizu, K., Sata, N., Ohishi, Y. (2010a), Electrical conductivities of pyrolitic mantle and MORB materials up to the lowermost mantle conditions, *Earth and Planetary Science Letters*, 289(3), 497-502.

Ohta, K, Hirose, K., Katsuya, S., Nagayoshi, S., Yasuo, O. (2010b), The electrical resistance measurements of $(Mg,Fe)SiO_3$ perovskite at high pressures and implications for electronic spin transition of iron, *Physics of the Earth Planetary Interiors*, 180(3-4), 154-158.

Ohtani, E. (2020), The role of water in Earth's mantle, *National Science Review*, 7(1), 224-232.

Ohtani, E., Litasov, K., Suzuki, A., Kondo, T. (2001), Stability field of new hydrous phase, δ-AlOOH, with implications for water transport into the deep mantle, *Geophysical Research Letters*, 28(20), 3991-3993.

Pamato, M. G., Myhill, R., Boffa Ballaran, T., Frost, D. J., Heidelbach, F., Miyajima, N. (2015), Lower-mantle water reservoir implied by the extreme stability of a hydrous aluminosilicate, *Nature Geoscience*, 8(1), 75-79.

Prescher, C., Prakapenka, V. B. (2015), DIOPTAS: a program for reduction of two-dimensional X-ray diffraction data and data exploration, *High Pressure Research*, 35(3), 223-230.

Sano-Furukawa, A., Komatsu, K., Vanpeteghem, C. B., Ohtani, E. (2008), Neutron diffraction study of δ-AlOOD at high pressure and its implication for symmetrization of the hydrogen bond, *American Mineralogist*, 93(10), 1558-1567.

Sano-Furukawa, A., Kagi, H., Nagai, T., Nakano, S., Fukura, S., Ushijima, D., et al. (2009), Change in compressibility of δ-AlOOH and δ-AlOOD at high pressure: A study of isotope effect and hydrogen-bond symmetrization, *American Mineralogist*, 94(8), 1255-1261.

Sano, A., Ohtani, E., Kubo, T., Funakoshi, K.-i. (2004), In situ X-ray observation of decomposition of hydrous aluminum silicate AlSiO 3OH and aluminum oxide hydroxide δ-AlOOH at high pressure and temperature, Journal of Physics and Chemistry of Solids, 65(8), 1547-1554.

Satta, N., Criniti, G., Kurnosov, A., Ballaran, T.B., Ishii, T., and Marquardt, H. (2021), High-Pressure Elasticity of δ-(Al,Fe)OOH Single Crystals and Seismic Detectability of Hydrous MORB in the Shallow Lower Mantle, *Geophysical Research Letters*, 48(23), e2021GL094185.

Spivak, A., Solopova, N., Cerantola, V., Bykova, E., Zakharchenko, E., Dubrovinsky, L., et al. (2014), Raman study of $MgCO_3$–$FeCO_3$ carbonate solid solution at high pressures up to 55 GPa, *Physics and Chemistry of Minerals*, 41(8), 633-638.

Su, X., Zhao, C., Xu, L., Lv, C., Song, X., Ishii, T., et al. (2021a), Spectroscopic evidence for the Fe^{3+} spin transition in iron-bearing δ-AlOOH at high pressure, *American Mineralogist*, 106(11), 1709–1716.

Su, X., Zhao, C., Lv, C., Zhuang, Y., Salke, N., Xu, L., et al. (2021b), The effect of iron on the sound velocities of δ-AlOOH up to 135 GPa, *Geoscience Frontiers*, 12(2), 937-946.

Suzuki, A., Ohtani, E., Kamada, T. (2000), A new hydrous phase δ-AlOOH synthesized at 21 GPa and 1000 °C, Physics and Chemistry of Minerals, 27(10), 689-693.

Tada, N., Baba, K., Utada, H. (2014), Three-dimensional inversion of seafloor magnetotelluric data collected in the Philippine Sea and the western margin of the northwest Pacific Ocean, *Geochemistry, geophysics, geosystems:* 15(7), 2895-2917.

Tarits, P., Mandéa, M. (2010), The heterogeneous electrical conductivity structure of the lower mantle, *Physics of the Earth Planetary Interiors*,183, 115-125.

Thompson, E. C., Campbell, A. J., and Tsuchiya, J. (2017), Elasticity of ε-FeOOH: Seismic implications for Earth's lower mantle, *Journal of Geophysical Research: Solid Earth*, 122, 5038-5047.

Thompson, E. C., Davis, A. H., Brauser, N. M., Liu, Z., Prakapenka, V. B., Campbell A. J. (2020), Phase transitions in ε-FeOOH at high pressure and ambient temperature, *American Mineralogist*, 105(12), 1769-1777.

Tsuchiya, J., Tsuchiya, T. (2011), First-principles prediction of a high-pressure hydrous phase of AlOOH, *Physical Review B*, 83(5), 054115.

Tsuchiya, J., Tsuchiya, T., Tsuneyuki, S., Yamanaka, T. (2002), First-principles calculation of a high-pressure hydrous phase, δ-AlOOH, *Geophysical Research Letters*, 29(19), 15-1-15-4.

Xu, C., Inoue, T. (2019), Melting of Al-Rich Phase D up to the Uppermost Lower Mantle and Transportation of H_2O to the Deep Earth, Geochemistry, Geophysics, Geosystems, 20(9), 4382-4389.

Wang, R., Yoshino, T. (2021), Electrical conductivity of diaspore, δ-AlOOH and ε-FeOOH, *American mineralogist*, 106(5), 774-781.

Zhuang, Y, Gan, B., Cui, Z., Tang, R., Tao, R., Hou, M., et al. (2022), Mid-mantle water transportation implied by the electrical and seismic properties of ε-FeOOH, *Science Bulletin*, 67(7), 748-754.

Figure Captions

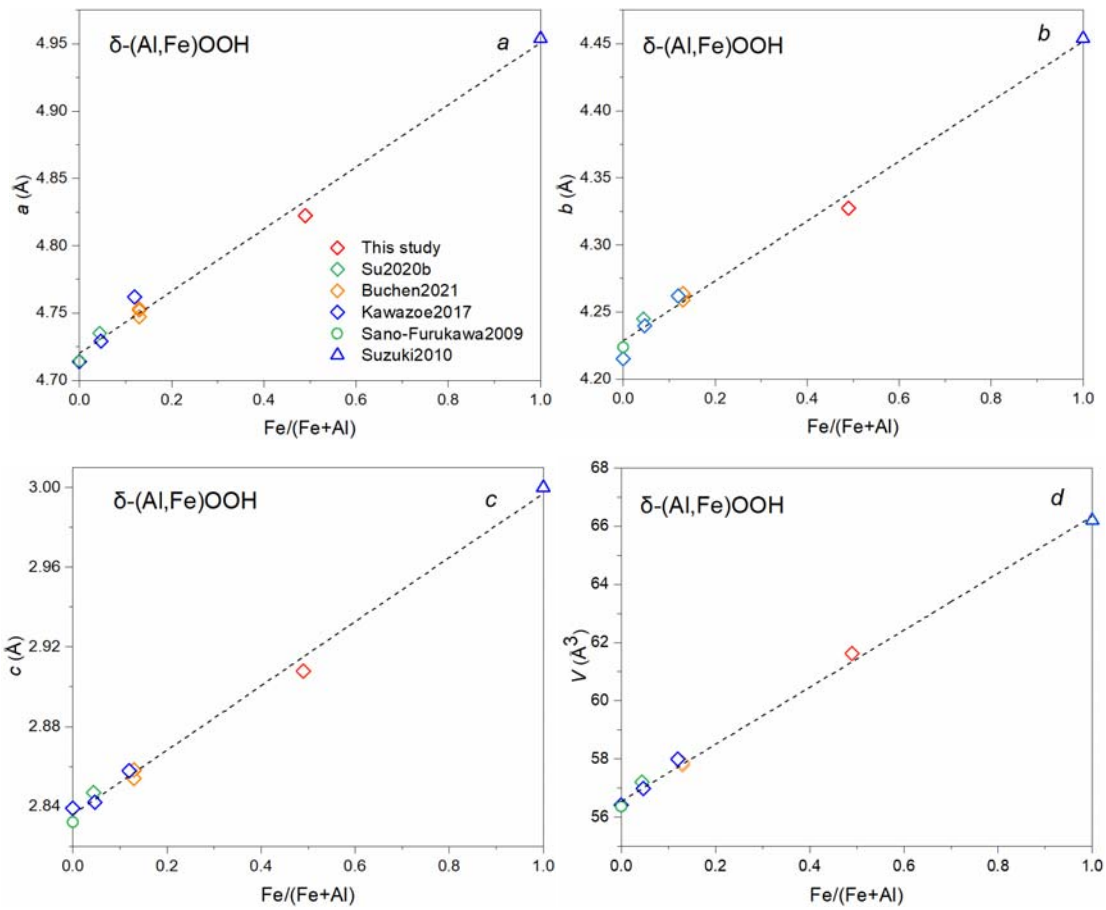

Figure 1. Unit-cell parameters of δ-(Al,Fe)OOH at ambient conditions. (***a***) *a*. (***b***) *b*. (***c***) *c*. (***d***) *V*. Red diamonds: δ-($Al_{0.52}Fe_{0.48}$)OOH, this study; green diamonds: δ-($Al_{0.95}Fe_{0.05}$)OOH, *Su et al.* (2021b); orange diamonds: δ-($Al_{0.87}Fe_{0.13}$)OOH, *Buchen et al.* (2021); blue diamonds: δ-AlOOH, δ-($Al_{0.832}Fe_{0.117}$)$OOH_{1.15}$, and δ-($Al_{0.908}Fe_{0.047}$)$OOH_{1.14}$, *Ohira et al.* (2019); green circles: δ-AlOOH, *Sano-Furukawa et al.* (2009); blue triangle: ε-FeOOH, *Suzuki et al.* (2010). Dashed lines connect the end-member values.

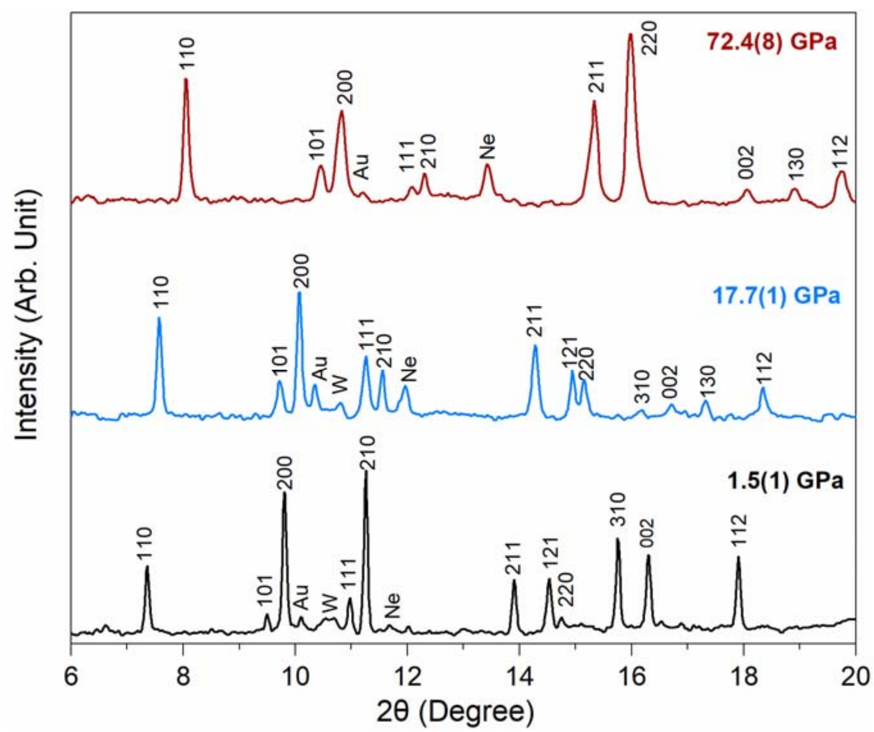

Figure 2. Representative X-ray diffraction patterns of δ-($Al_{0.52}Fe_{0.48}$)OOH at high pressure and 300 K. The equation of state of Au was used to determine pressure and its uncertainty (*Fei et al.,* 2007). Neon was used as the pressure medium. W indicates the diffraction lines of the tungsten gasket. The wavelength of the monochromatic X-ray beam was 0.4133 Å (corresponding to an X-ray energy of 30.0 keV).

DOI: https://doi.org/10.2138/am-2022-8393. http://www.minsocam.org/

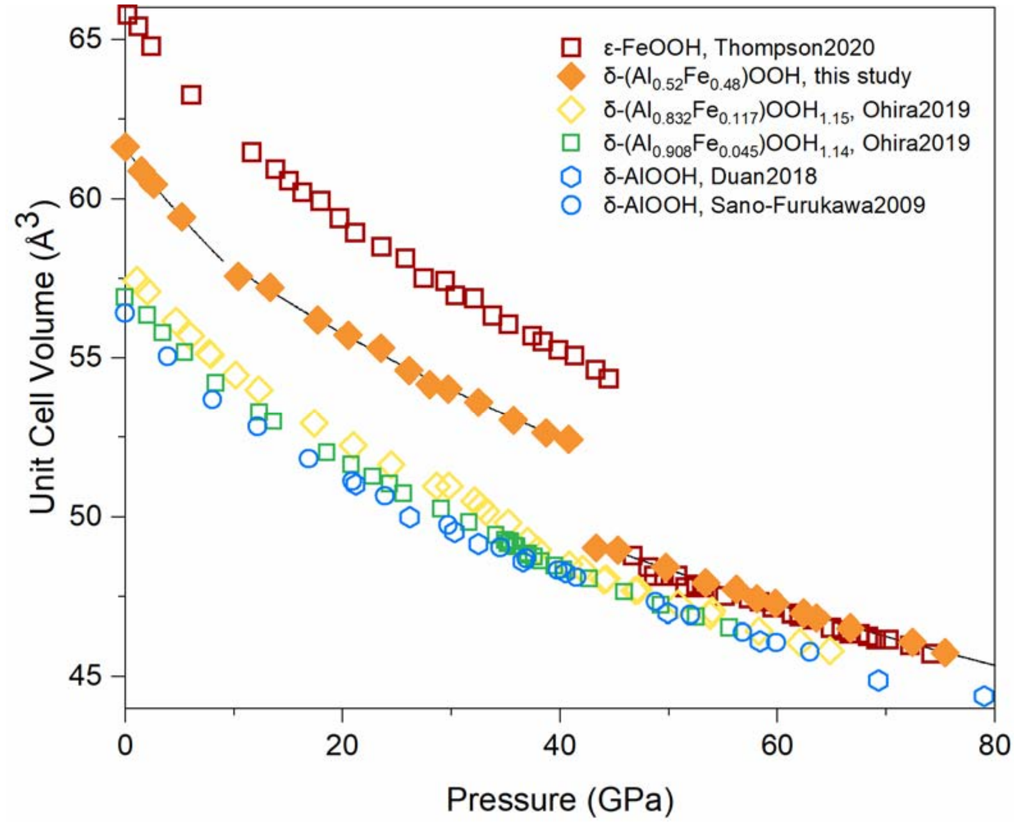

Figure 3. Pressure-volume relations of δ-(Al,Fe)OOH at high pressure and 300 K. Solid orange diamonds: experimental measurements of δ-($Al_{0.52}Fe_{0.48}$)OOH, this study; black curves: the 3rd Birch-Murnaghan (BM) EoS fits to the experimental data at 0–10.4, 13.3–40.8, and 43.3–75.4 GPa, respectively, this study; yellow diamonds and green squares: δ-($Al_{0.832}Fe_{0.117}$)$OOH_{1.15}$ and δ-($Al_{0.908}Fe_{0.047}$)$OOH_{1.14}$, respectively, *Ohira et al.* (2019); red squares: ε-FeOOH, *Thompson et al.* (2020); blue circles and hexagons: δ-AlOOH, *Sano-Furukawa et al.* (2009) and *Duan et al.* (2018), respectively. Errors for the Delta52 are smaller than the symbols and are not shown for clarity.

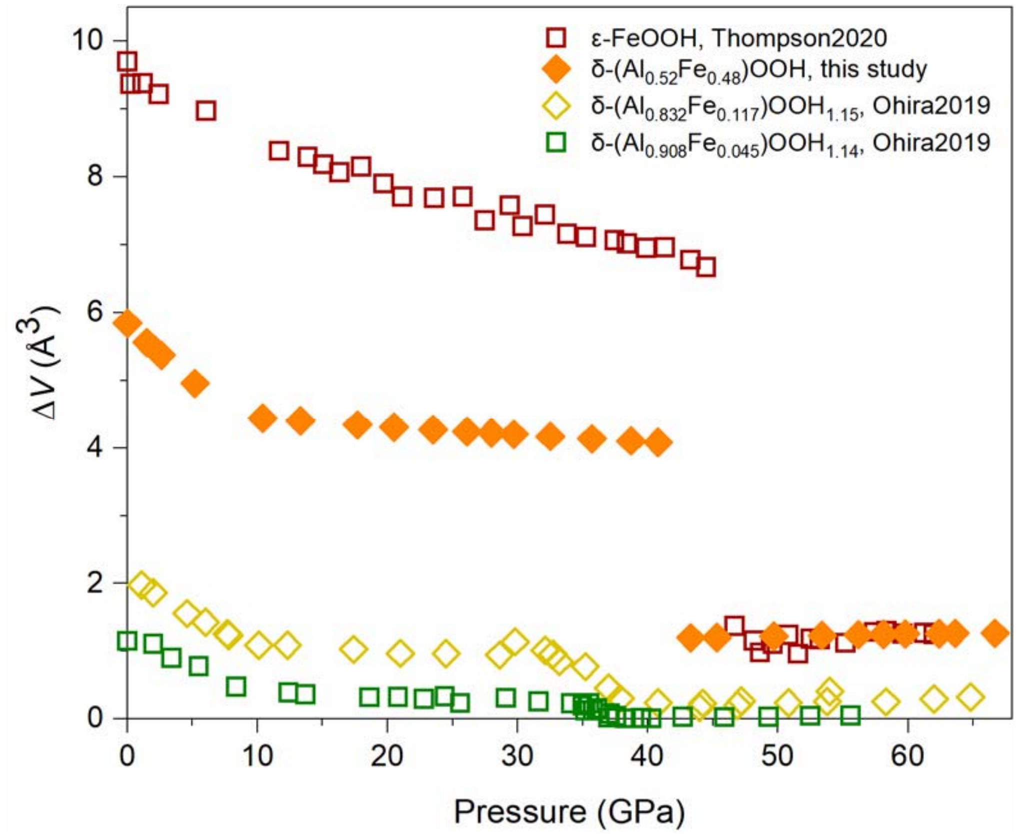

Figure 4. The unit cell volume difference (ΔV) between δ-(Al,Fe)OOH and pure δ-AlOOH at high pressure. The equation of state for δ-AlOOH is from *Sano-Furukawa et al.* (2009). A sharp discontinuity was observed in δ-($Al_{0.52}Fe_{0.48}$)OOH (denoted as "Delta52") across the spin transition of iron. Yellow diamonds and green squares: δ-($Al_{0.832}Fe_{0.117}$)$OOH_{1.15}$ and δ-($Al_{0.908}Fe_{0.047}$)$OOH_{1.14}$, respectively, *Ohira et al.* (2019); red squares: ε-FeOOH, *Thompson et al.* (2020). Errors for the Delta52 are smaller than the symbol size and are not be shown for clarity.

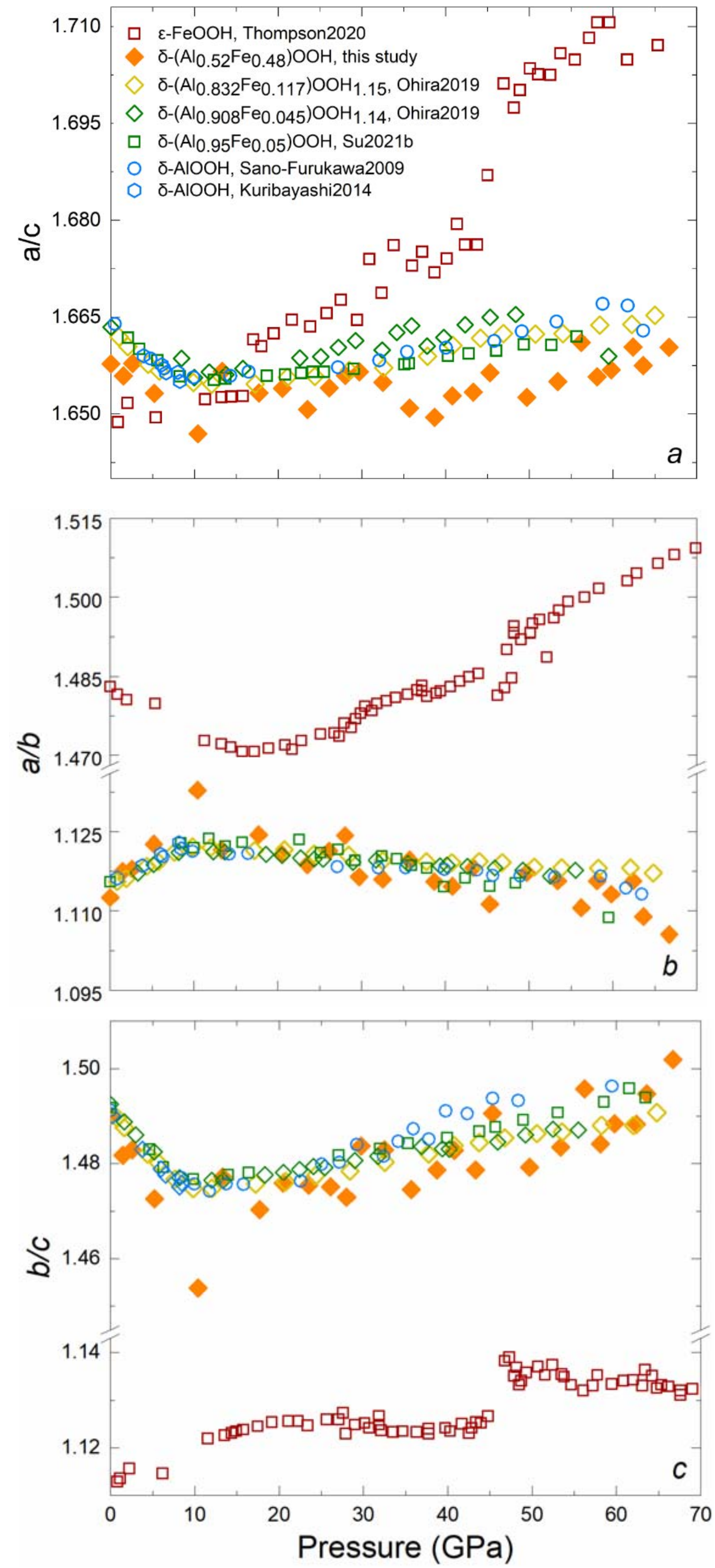
ε-FeOOH, Thompson2020
δ-(Al0.52Fe0.48)OOH, this study
δ-(Al0.832Fe0.117)OOH1.15, Ohira2019
δ-(Al0.908Fe0.045)OOH1.14, Ohira2019
δ-(Al0.95Fe0.05)OOH, Su2021b
δ-AlOOH, Sano-Furukawa2009
δ-AlOOH, Kuribayashi2014
a/c
a
a/b
b
b/c
c
Pressure (GPa)

DOI: https://doi.org/10.2138/am-2022-8393. http://www.minsocam.org/

Figure 5. Axial ratios as a function of pressure for δ-(Al,Fe)OOH. The axial ratio values of δ-$(Al_{0.52}Fe_{0.48})OOH$ undergo discontinuity at approximately 10 GPa, in good agreement with the two new Raman bands observed in this sample at 8.5–15.8 GPa by *Su et al.* (2021a). Yellow diamonds and green squares: δ-$(Al_{0.832}Fe_{0.117})OOH_{1.15}$ and δ-$(Al_{0.908}Fe_{0.047})OOH_{1.14}$, respectively, *Ohira et al.* (2019); red squares: ε-FeOOH, *Thompson et al.* (2020); blue circles and hexagons: δ-AlOOH, *Sano-Furukawa et al.* (2009) and *Kuribayashi et al.* (2014), respectively. Errors for the Delta52 are smaller than the symbol size and are not be shown for clarity.

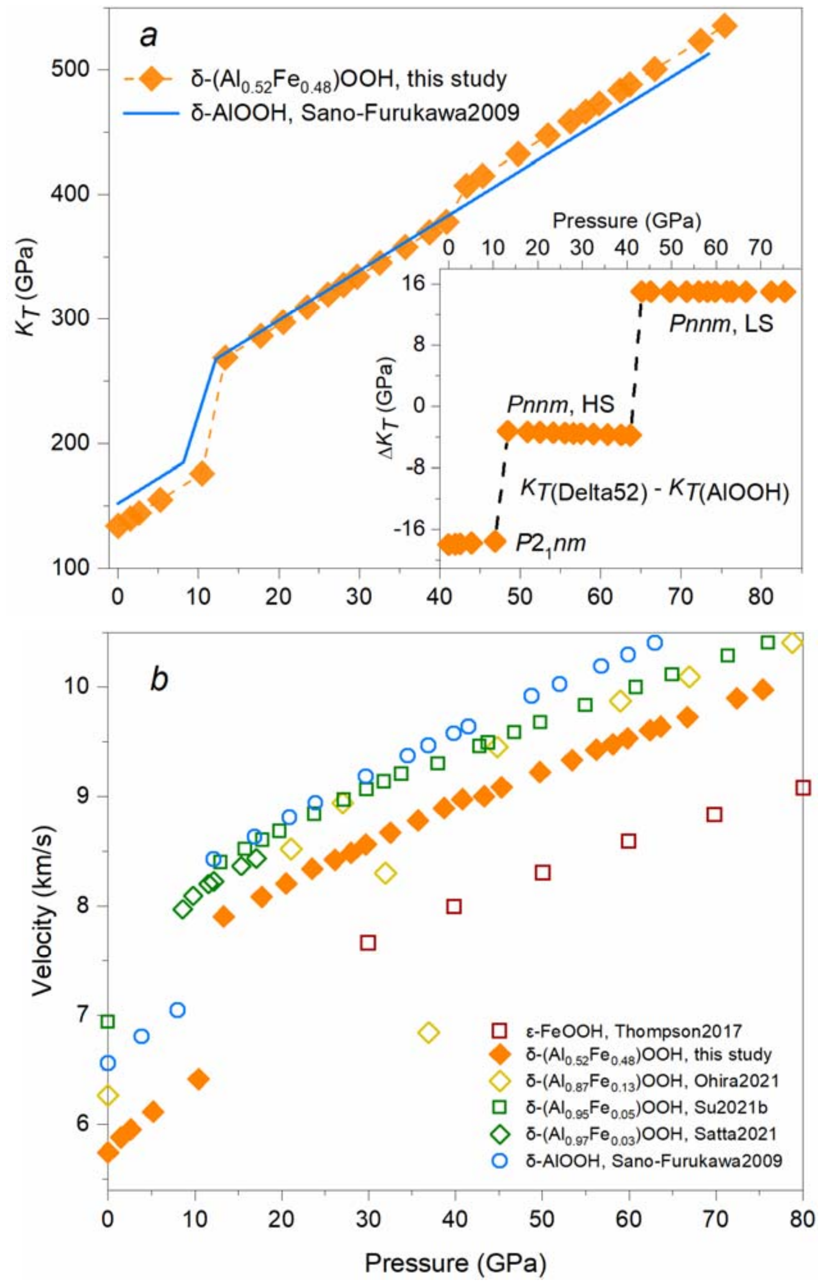

Figure 6. Isothermal bulk modulus (K_T) (***a***) and bulk sound velocities (***b***) of δ-(Al,Fe)OOH as a function of pressure at 300 K. Inset: the isothermal bulk modulus difference (ΔK_T) between δ-($Al_{0.52}Fe_{0.48}$)OOH and pure δ-AlOOH at high pressure. Orange solid diamonds: δ-($Al_{0.52}Fe_{0.48}$)OOH, this study; blue curve and open circles: δ-AlOOH, *Sano-Furukawa et al.* (2009); yellow diamonds: δ-($Al_{0.87}Fe_{0.13}$)OOH, *Ohira et al.* (2021); green squares: δ-($Al_{0.95}Fe_{0.05}$)OOH, *Su et al.* (2021b); green diamonds: δ-($Al_{0.97}Fe_{0.03}$)OOH, *Satta et al.* (2021).

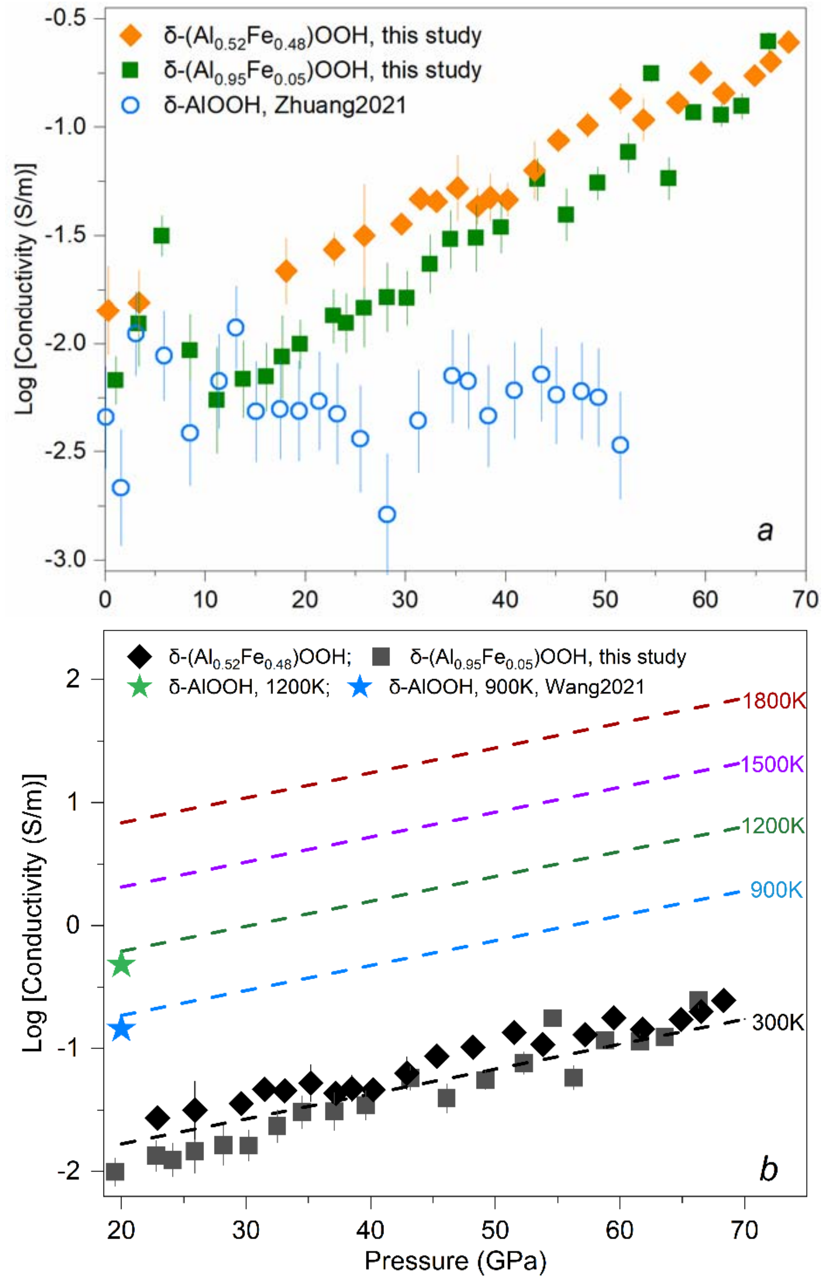

Figure 7. Electrical conductivity of the δ-(Al,Fe)OOH phase as a function of pressure at room temperature (***a***) and high temperature (***b***). Solid squares and diamonds: δ-($Al_{0.95}Fe_{0.05}$)OOH and δ-($Al_{0.52}Fe_{0.48}$)OOH, this study; open circles: δ-AlOOH, *Zhuang et al.* (2021); star symbols: δ-AlOOH at 900 K (blue) and 1200 K (olive), *Wang and Yoshino* (2021); dashed curves: the EC fits at 300 K (black), 900 K (blue), 1200 K (olive), 1500 K (purple), and 1800 K (red), respectively. Vertical ticks represent the uncertainties for pure and iron-bearing δ-AlOOH.

This is the peer-reviewed, final accepted version for American Mineralogist, published by the Mineralogical Society of America.
The published version is subject to change. Cite as Authors (Year) Title. American Mineralogist, in press.
DOI: https://doi.org/10.2138/am-2022-8393. http://www.minsocam.org/

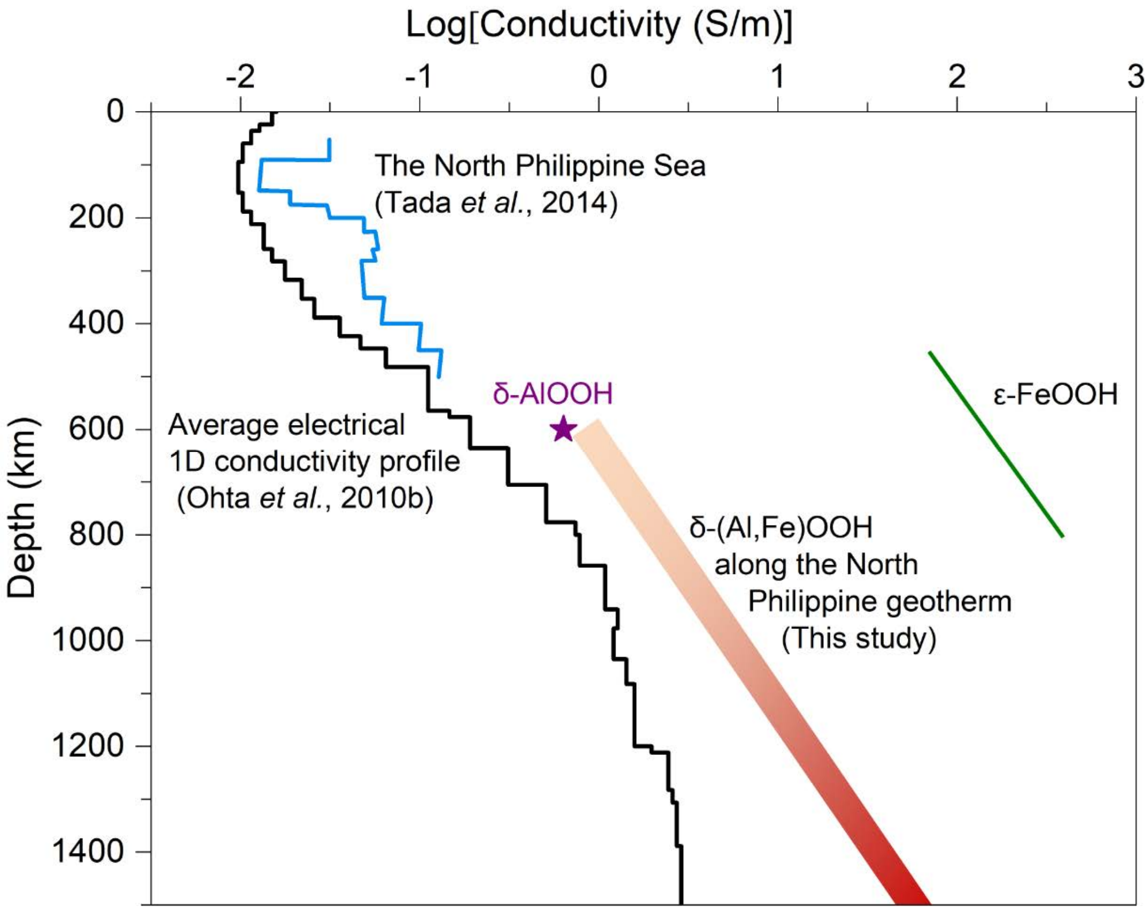

Figure 8. The conductivity-depth profile of the δ-(Al,Fe)OOH phase along the North Philippine geotherm. The orange-red envelope is a 95% confidence interval for the EC values of the δ-(Al,Fe)OOH phase. Blue curve: the conductivity-depth profile of the North Philippine Sea, *Tada et al.* (2014); black curve: average electrical 1D conductivity profile, *Ohta et al.* (2010b); purple star symbol: the electrical conductivity of δ-AlOOH at 20 GPa, *Wang and Yoshino* (2021); olive curve: the conductivity-depth profile of ε-FeOOH along the North Philippine geotherm, *Wang and Yoshino* (2021).

Table 1. Lattice parameters of δ-($Al_{0.52}Fe_{0.48}$)OOH at high pressure and 300 K

P (GPa)	*a* (Å)	*b* (Å)	*c* (Å)	*V* (Å^3)
0.0(0)	4.8440(3)	4.3540(5)	2.9220(6)	61.63(1)
1.5(1)	4.8298(8)	4.3220(2)	2.9167(5)	60.88(3)
2.6(1)	4.8208(8)	4.3122(2)	2.9079(5)	60.45(3)
5.2(1)	4.7958(7)	4.2718(2)	2.9009(4)	59.43(3)
10.4(1)	4.7534(1)	4.1960(1)	2.8862(7)	57.57(7)
13.3(1)	4.7371(2)	4.2238(8)	2.8595(7)	57.22(7)
17.7(1)	4.7095(1)	4.1884(1)	2.8486(7)	56.19(7)
20.5(2)	4.6918(6)	4.1866(9)	2.8367(4)	55.72(3)
23.5(1)	4.6748(7)	4.1786(1)	2.8320(6)	55.32(3)
26.1(1)	4.6616(6)	4.1571(8)	2.8183(4)	54.62(3)
28.0(2)	4.6548(6)	4.1402(1)	2.8109(4)	54.17(3)
29.7(2)	4.6404(9)	4.1564(9)	2.8013(6)	54.03(7)
32.5(3)	4.6263(9)	4.1454(8)	2.7955(6)	53.61(6)
35.7(3)	4.6115(9)	4.1187(7)	2.7933(6)	53.05(6)
38.7(5)	4.5925(9)	4.1168(7)	2.7842(6)	52.64(6)
40.8(7)	4.5882(9)	4.1162(1)	2.7760(5)	52.43(6)
43.3(7)	4.4921(8)	4.0173(4)	2.7169(5)	49.03(6)
45.3(8)	4.4834(8)	4.0344(4)	2.7067(5)	48.96(6)
49.7(8)	4.4714(8)	4.0022(4)	2.7057(5)	48.42(6)
53.4(7)	4.4563(8)	3.9942(4)	2.6926(5)	47.93(6)
56.2(6)	4.4487(8)	4.0057(3)	2.6782(9)	47.73(6)
58.1(6)	4.4414(5)	3.9810(5)	2.6824(4)	47.43(2)
59.8(6)	4.4349(5)	3.9840(4)	2.6767(8)	47.29(2)
62.4(6)	4.4314(5)	3.9720(3)	2.6689(8)	46.98(2)
63.6(7)	4.4156(8)	3.9818(3)	2.6640(9)	46.84(6)
66.7(8)	4.4034(7)	3.9830(2)	2.6521(8)	46.52(6)
72.4(8)	4.3872(7)	3.9773(2)	2.6413(8)	46.09(5)
75.4(9)	4.3790(7)	3.9565(1)	2.6411(8)	45.76(5)

Table 2. Equation of state parameters of δ-($Al_{0.52}Fe_{0.48}$)OOH at 300 K.

Composition	V_0 (Å^3)	K_0 (GPa)	K_{T0}'	EoS	*P* range	References
δ-($Al_{0.52}Fe_{0.48}$)OOH[h]	61.6(1)	134 (4)	4 (fixed)	2nd BM	0.0–10.4	This study
δ-($Al_{0.52}Fe_{0.48}$)OOH[l]	60.4(1)	216 (2)	3.98(9)	3rd BM	13.3–40.8	This study
δ-($Al_{0.52}Fe_{0.48}$)OOH[j]	56.5(1)	234 (2)	4.00(2)	3rd BM	43.3–75.4	This study
δ-($Al_{0.832}Fe_{0.117}$)$OOH_{1.15}$[h]	57.85(2)	147(1)	4 (fixed)	2nd BM	1.1–10.1	Ohira et al. (2019)
δ-($Al_{0.832}$($Fe_{0.117}$)$OOH_{1.15}$	55.2(4)	241(14)	4 (fixed)	SC EoS	36.1–64.8	Ohira et al. (2019)
δ-($Al_{0.908}Fe_{0.045}$)$OOH_{1.14}$[h]	57.03(7)	152(7)	4 (fixed)	2nd BM	0.0–8.4	Ohira et al. (2019)
δ-($Al_{0.908}Fe_{0.045}$)$OOH_{1.14}$	55.4(3)	223(11)	4 (fixed)	SC EoS	34.9–55.6	Ohira et al. (2019)
δ-AlOOH[a]	56.408(9)	152(2)	4 (fixed)	2nd BM	0.0–10.0	Sano-Furukawa et al. (2009)
δ-AlOOH[b]	55.47(8)	219(3)	4 (fixed)	2nd BM	10.0–63.5	

[a] *P*2_1*nm* at the high-spin state of δ-AlOOH; [b] *Pnnm* at the high-spin state of δ-AlOOH; [h] *P*2_1*nm* at the high-spin state of δ-(Fe,Al)OOH; [l] *Pnnm* at the high-spin state of δ-(Fe,Al)OOH; [j] *Pnnm* at the low-spin state of δ-(Fe,Al)OOH; SC EoS= Spin crossover EoS; BM = Birch-Murnaghan.

Table 3. Volume collapse of δ-(Al,Fe)OOH across the spin transition at room temperature.

Composition	PTM[a]	Pressure calibrant	Spin crossover (GPa)	Volume collapse	Reference
δ-$(Al_{0.52}Fe_{0.48})OOH$	Ne	Au	41–45	6.5%	This study
δ-$(Al_{0.95}Fe_{0.05})OOH$	Ne	Au	30-42	1.3%	Su et al. (2021b)
δ-$(Al_{0.908}Fe_{0.045})OOH_{1.14}$	Ne	Ruby	32–40	1.3%	Ohira et al. (2019)
δ-$(Al_{0.832}Fe_{0.117})OOH_{1.15}$	He	Ruby	32–40	2.8%	Ohira et al. (2019)
ε-FeOOH	Ne	Ruby	~45(2)	10.3%	Thompson et al. (2020)

[a] PTM: Pressure-transmitting medium.

Table 4. The electrical conductivity of iron-bearing δ-AlOOH at high pressures and 300 K.

δ-($Al_{0.95}Fe_{0.05}$)OOH		δ-($Al_{0.52}Fe_{0.48}$)OOH	
P (GPa)	Log[*σ*(S/m)]	*P* (GPa)	Log[*σ*(S/m)]
1.1(1)	-2.17(32)	0.3(1)	-1.84(27)
3.4(3)	-1.90(28)	3.4(4)	-1.80(26)
5.7(6)	-1.50(22)	18.1(19)	-1.66(24)
8.5(9)	-2.03(31)	22.9(25)	-1.56(23)
11.2(11)	-2.26(33)	25.9(28)	-1.49(22)
13.8(15)	-2.16(32)	29.6(32)	-1.44(21)
16.1(17)	-2.15(32)	31.5(34)	-1.33(19)
17.7(19)	-2.06(31)	33.1(36)	-1.34(21)
19.5(21)	-2.00(31)	35.2(38)	-1.28(19)
22.8(25)	-1.87(28)	37.2(41)	-1.36(21)
24.1(26)	-1.90(27)	38.5(42)	-1.32(19)
25.9(28)	-1.83(26)	40.2(44)	-1.33(21)
28.2(31)	-1.78(23)	42.9(47)	-1.19(18)
30.2(33)	-1.78(24)	45.3(49)	-1.06(16)
32.5(35)	-1.63(22)	48.2(53)	-0.98(14)
34.5(37)	-1.51(23)	51.5(56)	-0.86(13)
37.1(41)	-1.51(22)	53.8(59)	-0.96(14)
39.6(43)	-1.46(19)	57.2(62)	-0.88(13)
43.2(47)	-1.24(21)	59.5(65)	-0.74(11)
46.1(51)	-1.40(18)	61.8(67)	-0.84(12)
49.2(54)	-1.25(19)	64.9(71)	-0.76(11)
52.3(57)	-1.11(16)	66.5(73)	-0.69(9)
54.6(61)	-0.75(11)	68.3(75)	-0.60(9)
56.3(62)	-1.23(18)		
58.8(64)	-0.93(14)		
61.6(67)	-0.94(13)		
63.6(69)	-0.90(15)		
66.3(71)	-0.60(9)		

Conductivity error was estimated by the following equation:

$\Delta\sigma \approx \sigma \frac{-d^2}{16D^2 \ln 2}$, where d is the electrode contact length, and D is the diameter of the sample. The uncertainty was estimated to be ~ 15%.